Metals and Materials International (2022) 28:1143–1156
https://doi.org/10.1007/s12540-021-00978-9

Improvement of Yield Asymmetry and Enhancement of Mechanical Properties of Extruded AZ110 Alloy with La-Rich Misch Metal Addition

Qiyu Liao[1] · Wenxin Hu[2] · Qichi Le[1] · Xingrui Chen[1] · Yanchao Jiang[1]

Received: 14 October 2020 / Accepted: 21 January 2021 / Published online: 11 June 2021

Abstract
In this paper, effects of the La-rich MM (Misch Metal) on the microstructure, texture and mechanical properties of extruded AZ110 alloy during tension and compression deformation were investigated. High strength and low tension–compression yield asymmetry of AZ110MM alloy (AZ110 alloy with La-rich MM addition) are developed by hot extrusion. The addition of La-rich MM brings Al-RE phases (Al_2(La, Ce) and Al_{11}(La, $Ce)_3$) to the as-cast AZ110 alloy, which play an important role in the grain refinement and texture weakening during extrusion deformation. Such grain refinement and texture weakening obviously inhibit the nucleation and growth of twins and make the deformation mechanism change from twinning to multiple slip during cold compression deformation. Furthermore, the Al-RE phases also improve the tension–compression yield asymmetry performance of the extruded AZ110 alloy via the combining effects of grain refinement, texture weakening and the transformation from twinning to multiple slip. Moreover, the extruded AZ110MM alloy shows much higher strength over AZ110 alloy, owning to texture effect, grain boundary strengthening and precipitation strengthening.

Keywords La-rich misch metal · AZ110 magnesium alloy · Tension–compression yield asymmetry · Texture evolution · Twinning · Mechanical properties

1 Introduction

Wrought magnesium alloys are very attractive in various industrial products because of their low density, excellent mechanical properties, good damping, strong electromagnetic shielding ability and recyclability [1]. Among various magnesium alloys, those alloys based on Mg–Al–Zn system are the most widely used wrought magnesium, due to their excellent mechanical properties and high productivity and good product qualities. Nevertheless, the application of Mg alloys is very limited due to their low absolute strength and elongation. AZ80 alloy has been widely used in commercial applications on account of their combination of strength and ductility at ambient temperature [2]. However, because the deformation behavior of magnesium alloy is different in the process of tension and compression deformation, its yield asymmetry is inevitable. Besides, in order to meet the requirements of large-scale applications, its strength needs to be further developed.

It has been found that the tension–compression yield asymmetry in Mg and Mg alloys is caused by the strong basal texture and twin asymmetry. The $\{10\bar{1}2\}$ extension twins are activated when the tensile direction is perpendicular to the c-axis or the compressive direction is parallel to the c-axis [3, 4]. The $\{10\bar{1}2\}$ extension twins are more likely to occur during compression for Mg alloys leading to low compressive yield strength [5]. However, the slipping-dominated tensile deformation can obtain relatively higher yield stress [5]. Tension–compression asymmetry is closely related to the anisotropy of Mg alloys, resulting in formability problems. Hence, the minimization of asymmetry effect is of prime importance in the quest for widespread commercial acceptability.

Adding RE elements can remarkably refine the microstructure and improve the mechanical properties of Mg alloys. It was reported that the yield asymmetry of Mg and Mg alloys could be improved through several methods, such as, severe plastic deformation, heat treatment

✉ Qichi Le
qichil@mail.neu.edu.cn

[1] Key Lab of Electromagnetic Processing of Materials, Ministry of Education, Northeastern University, Shenyang 110819, China

[2] Baotou Research Institute of Rare Earths, Baotou 014000, China

and alloying with RE elements [6, 7]. When alloying with RE elements in Mg alloys, RE phases with good thermal stability precipitate in the matrix, which can tangle dislocations and boost recrystallization nucleation during deformation. Quan Zhang, et al. [8] found that alloying RE elements could reduce the stacking fault energies of Mg or Mg alloys and further facilitate DRX (dynamic recrystallization). Additionally, RE elements can also reduce the critical resolute shear stress (CRSS) of Mg alloys, leading to the activation of some prismatic slips and the weakening of the basal texture [9]. The main strengthening phase in the AZ110 alloy is $Mg_{17}Al_{12}$. Mónica et al. [10] stated that this hard and brittle $Mg_{17}Al_{12}$ phase results in poor formability and tension–compression yield symmetry. However, the addition of trace RE elements can improve the mechanical properties and formability of Mg–Al–Zn alloys [11–14]. Alloying with RE elements is the simplest and most direct method to improve the mechanical properties of AZ110 alloy without request for special equipment and unconventional processing methods.

The previous works were mainly based on the methods of severe plastic deformation and annealing to study the tension and compression yield asymmetry of magnesium alloys. In addition, there are many researches on the microstructure evolution and mechanical properties of Mg–Al–Zn alloys with different RE contents, but few researches on the effects of La-rich MM on the microstructure and mechanical properties of AZ110 alloy. Based on previous studies, this study attempts to use the conventional reverse extrusion method to enhance the strength and improve the tension–compression asymmetry of extruded AZ110 alloy by adding light and cheap RE (1.84 wt% La-rich MM). The grain size, twinning behavior, precipitations and texture of the extruded AZ110 and AZ110MM alloys were thoroughly studied and analyzed. Additionally, the tension–compression properties of the investigated alloys were tested and analyzed. Finally, effect of the La-rich MM addition on the microstructure and mechanical properties of the AZ110 alloy were discussed. Such an investigation will provide an important basis for improving the mechanical properties of AZ110 alloy and provide a guideline for the wide application of this promising magnesium alloy in the industry.

2 Experimental Procedure

The magnesium alloy studied in this work is traditional AZ110 magnesium alloy with the addition of a small amount of La-rich MM. Pure Mg, Al, Zn, $MnCl_2$, and Mg–30% La-rich MM (La: Ce = 2: 1) were prepared to melt in a high-temperature resistance furnace at 973–1013 K in a CO_2 and SF_6 protective gas atmosphere. The chemical compositions of the experimental alloys determined by inductively coupled plasma (ICP) analyzer are listed in Table 1. For simplicity, the alloys Mg–10.8Al–0.44Zn–0.11Mn and Mg–10.5Al–0.40Zn–0.08Mn–1.22La–0.62Ce are expressed as AZ110 and AZ110MM, respectively. Then, the ingots were machined into round bars with a diameter of 70 mm and further homogenized in a muffle furnace at 673 K for 20 h. The round bars were reheated at 573 K for 60 min and extruded at the same temperature with extrusion ratio of 17:1 and extrusion speed of 1.0 mm/s.

The microstructural characteristics of the extruded alloys were investigated in the ED–TD (extrusion direction–transverse direction) plane observed with optical microscopy (OM) and a scanning electron microscopy (SEM) instrument equipped with an energy dispersive X-ray spectroscopy (EDS) spectrometer. The pole figure contained three crystallographic planes (0002), $(10\bar{1}0)$ and $(1\bar{2}10)$. Electron backscattered diffraction (EBSD) analysis was implemented on a JEOL 733 electron probe equipped with an HKL-EBSD system. Texture was tested by EBSD. Transmission electron microscopy (TEM) was used to image microscopic features. The tensile mechanical properties of the extrusion bars were tested at room temperature using a SANS CMT-5105 material tensile prototype at a strain rate of 1.0 mm min^{-1}. The samples were stretched up to a strain of 5%. The compression mechanical properties of the extrusion bars were tested at room temperature using a Gleeble 2000 compression testing machine with a compressive stretching rate of 0.3 mm min^{-1}. The samples were stretched up to strains of 2% and 4%. The extruded and Tens-5% (5% tensile deformation) samples and Comp-2% and 4% (2% and 4% compressive deformation) samples were studied to examine the tensile-compressive deformation behaviors. The loading directions of the tensile and compressive specimens were parallel to the extrusion direction.

Table 1 Chemical compositions of the two experimental alloys (wt%)

Designation	Al	Zn	Mn	Fe	La	Ce	Mg
AZ110	10.8	0.44	0.11	< 0.003	–	–	Bal
AZ110MM	10.5	0.40	0.08	< 0.003	1.22	0.62	Bal

3 Results

3.1 Phase Characteristics

As shown in Fig. 1, SEM and EDS tests were used to identify the secondary phases. The possible secondary phases were determined by the XRD test. The main phase of the AZ110 alloy is brittle and rigid $Mg_{17}Al_{12}$ phase (Fig. 1c), which is mainly characterized by discontinuous distribution network (Fig. 1a). With the addition of La-rich MM, the microstructure of AZ110 alloy is refined and the dendrite arm spacing is shortened. Combined with previous studies [5], it can be revealed that the AZ110MM alloy is mainly composed of a-Mg, $Mg_{17}Al_{12}$ (gray blocks), and Al–(La, Ce) phases (bright blocks or long strip shape), seen in Figs. 1 and 2b. According to the corresponding EDS results (see Fig. 2d–f), the RE-rich phases can be identified as Al_2(La, Ce) and Al_{11}(La, Ce)$_3$, and the gray phase is $Mg_{17}Al_{12}$. This is consistent with the findings of

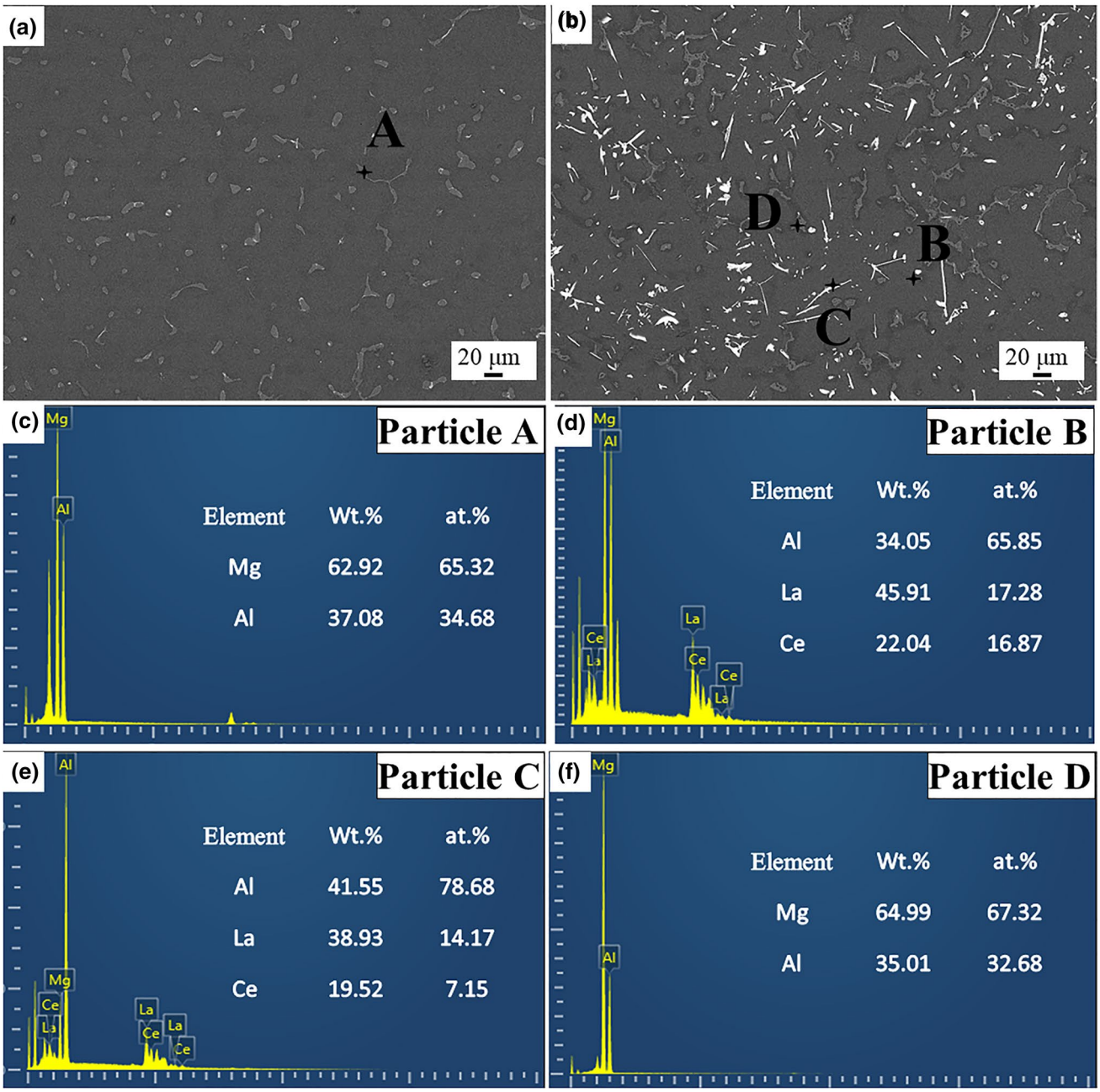

Fig. 1 SEM images of the as-cast samples. **a** AZ110 alloy; **b** AZ110MM alloy; **c–f** the corresponding EDS results of the secondary phases

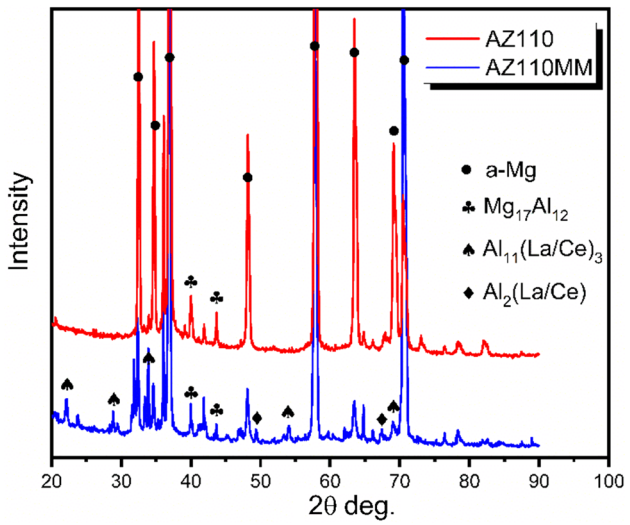

Fig. 2 XRD patterns of the as-cast AZ110 and AZ110MM alloys

Nami et al. [12, 13]. As shown in Fig. 2b, the bright block phase (particle B) is $Al_2(La, Ce)$, and the bright strip phase (particle C) is $Al_{11}(La, Ce)_3$.

In order to clarify the secondary phase in the extruded AZ110MM alloy, the corresponding EDS results and typical topography maps of the typical precipitated phases are shown in Fig. 3. As we can see in Fig. 3a, b, the Al-RE phases show block distribution with size less than 1 μm in the matrix. Both the two phases contain the elements Al, La and Ce. The SAED patterns and EDS compositions in Fig. 3c, d are for the phase marked with red box in the Fig. b. The precipitated phases in Fig. 3b can be identified as $Al_2(La, Ce)$. The above results coincide well with the results of the as-cast AZ110MM alloy. It can be concluded that there is no phase transition in the extrusion process.

3.2 Microstructure Evolution During Compression and Tension

Figure 4 presents the EBSD images and misorientation distribution maps of the extruded AZ110 and AZ110MM alloys under compression. It can be seen from Fig. 4a, g that the initial extruded AZ110 and AZ110MM alloys present fine equiaxed grains. The average grain size of the AZ110MM alloy is 1.1 μm, which is smaller than that of AZ110 alloy. It can be seen that the La-rich MM has a

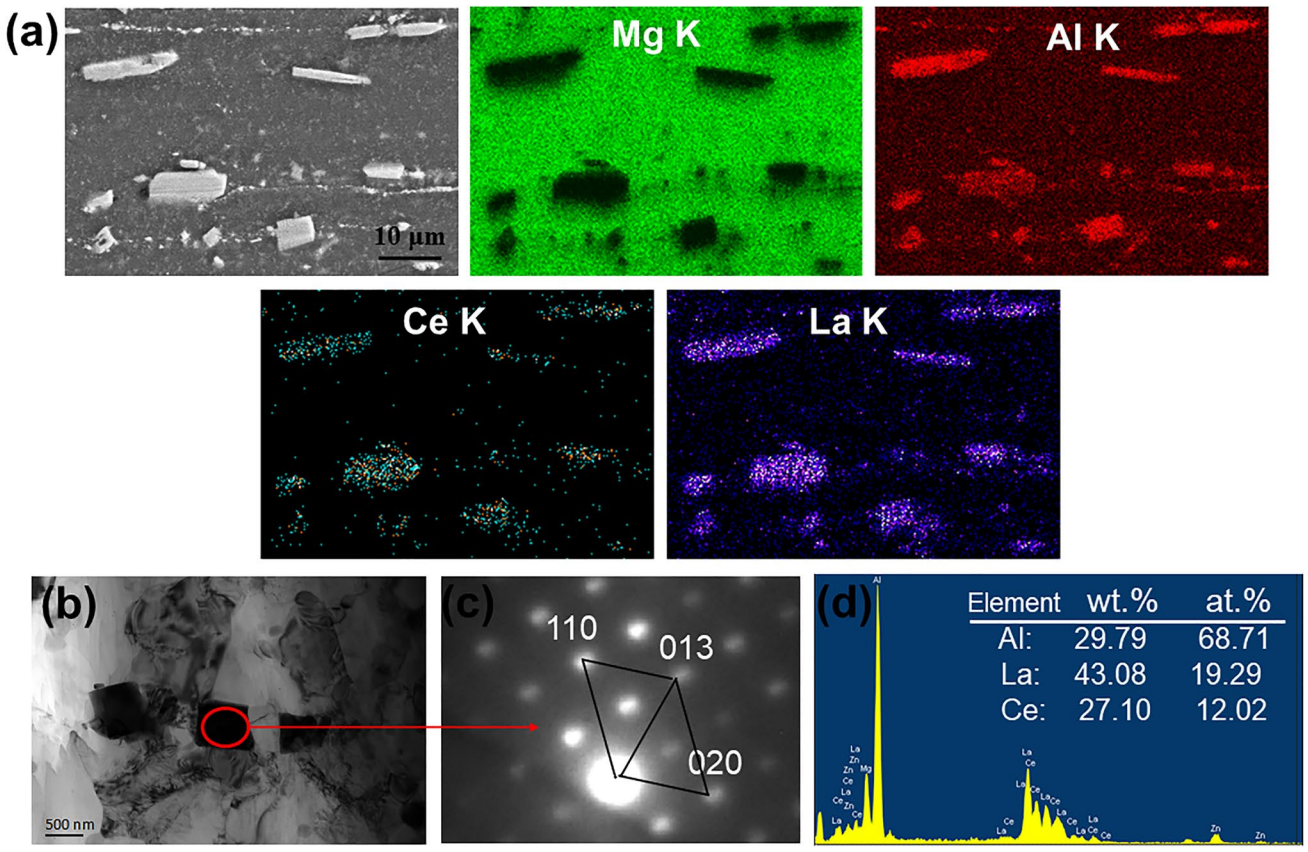

Fig. 3 **a** EDS images of the secondary phases in the extruded AZ110MM alloy; TEM images of the typical RE phase: **b** Bright-field graph; **c** patterns by SAED; **d** compositions by EDS

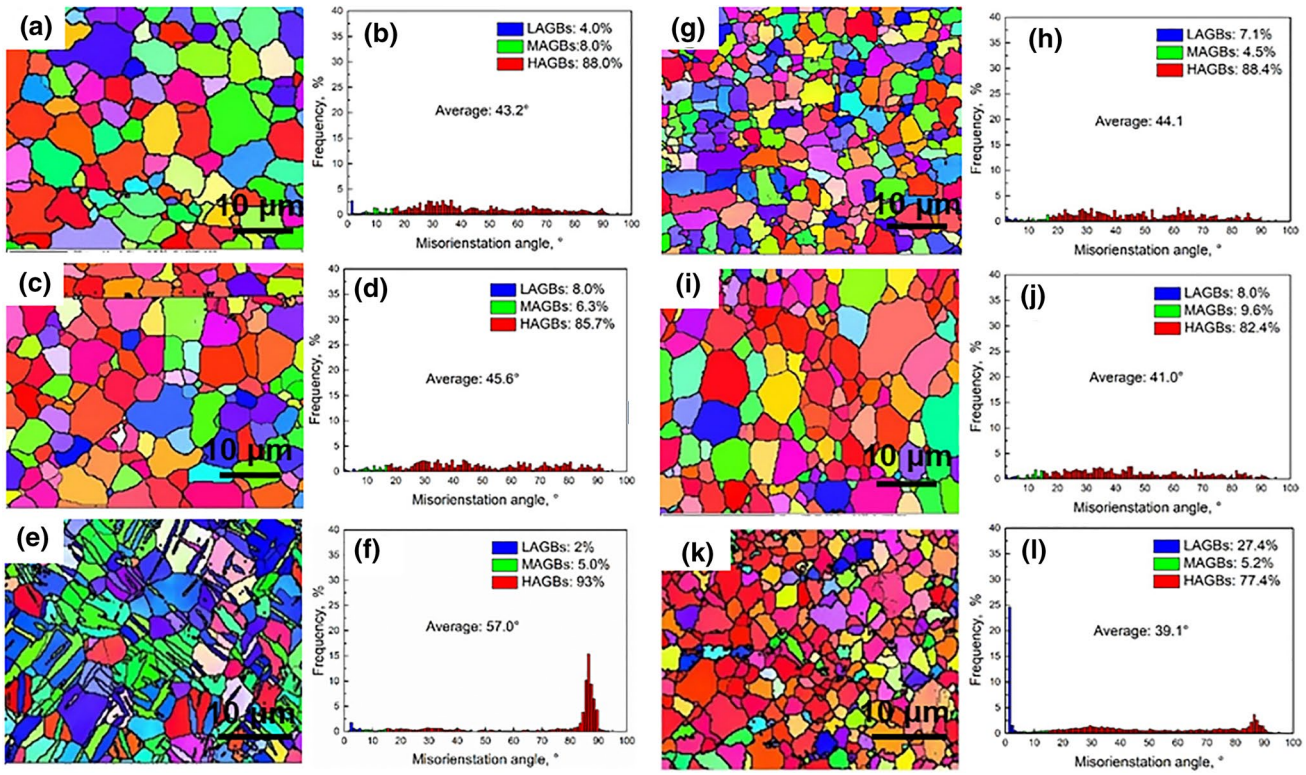

Fig. 4 EBSD images and misorientation distribution maps of the extruded AZ110 and AZ110MM alloys during compression. AZ110 alloy: **a**, **b** initial extruded state; **c**, **d** 2% compressive strain; **e**, **f** 4% compressive strain. AZ110MM alloy: **g**, **h** initial extruded state; **i**, **j** 2% compressive strain; **k**, **l** 4% compressive strain

significant effect on the grain refinement of AZ110 alloy during extrusion. The grains with misorientation angles between 5° and 15° are MAGBs (middle angle grain boundaries), and the misorientation angle of LAGBs (low angle grain boundaries) is less than 5°. The misorientation angle of the HAGBs (high angle grain boundaries) exceeds 15°. As shown in Fig. 4b, h, the misorientation orientation angles of the initial extruded alloys are focused on HAGBs, and the distribution proportion of LAGBs and MAGBs is extremely low. With increasing compressive deformation of AZ110 and AZ110MM alloys, as seen in Fig. 4c, d, i, j, the LAGBs slightly increase. The fluctuation in the fraction of LAGBs corresponds to DRX nucleation after deformation increases. With the compressive strain further increasing, as shown in Fig. 4e, f, k, l, a large number of twins nucleate and grow in the coarse grain of the AZ110 alloy, while there are no twins in the AZ110MM alloy. Furthermore, the misorientation angles gradually focus around the HAGBs (about 86°), and the proportion of LAGBs decreases in AZ110MM alloy. While the fraction of LAGBs in AZ110 MM alloy increase obviously and the ratio of HAGBs decreased. As shown in Fig. 5, there are a few twins nucleate in the AZ110 alloy and no twins in AZ110 MM alloy during tension. The above results show that when a load is applied along the ED, twins are more easily formed during compression than tension.

Twinning is an important characteristic of AZ110 alloy during compression, so it is necessary to analyze the twins separately. The EBSD results of AZ110 alloy under 4% compressive deformation are shown in Fig. 6. The corresponding special boundary map (Fig. 6b) reveals that most of the twins are identified as $\{10\bar{1}2\}$ extension twins. It can be seen that the $\{10\bar{1}2\}$ extension twins have an obvious effect on the texture type and grain orientation. Therefore, the texture characteristics of the twins and their parent crystals are worth studying. In the selected grains (Fig. 6a), T2 and T3 represent $\{10\bar{1}2\}$ extension twins, T1 represents $\{10\bar{1}2\}$–$\{10\bar{1}2\}$ double extension twins and grain P represents their parent grain. As shown in Fig. 6c, the misorientation angle shows a peak value at 86°. The three-dimensional crystallographic relationship between the selected $\{10\bar{1}2\}$ extension twins and their corresponding parent grain are showed in Fig. 6d. As shown in Fig. 6e, f, the c-axes of the $\{10\bar{1}2\}$ extension twins are tilted in the compression direction, forming the (0001) basal texture. Meanwhile, the c-axis of their parent grain is aligned in the TD with an evident cluster at $<10\bar{1}0>$ ∥ED. The above results indicate that some parent grains

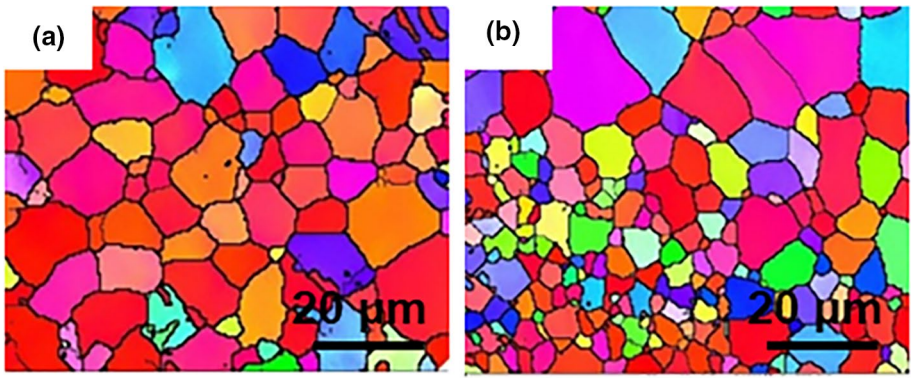

Fig. 5 EBSD images of the extruded AZ110 and AZ110MM alloys under 5% tensile strain. **a** AZ110 alloy; **b** AZ110MM alloy

change their texture direction by forming twins, while the other parent grains transform their c-axis from parallel to ND to parallel to TD by grain rotation.

3.3 Texture Evolution

Figure 7 shows the pole figures of the extruded AZ110 and AZ110MM alloys during compression and tension. As shown in Fig. 7a, the extruded AZ110 alloy presents a typical (0001) fiber texture on the ED–TD plane with relatively random basal texture. The texture components are not concentrated in a particular region but distributed along the TD and the maximum texture intensity value is 11.94. As we can see in Fig. 7b, as the compressive strain increases to 2%, the pole density points in the (0001) pole figure are distributed along the TD. When the compressive strain is 4% (Fig. 7c), parts of the coarse grains nucleate twins and the pole density points of the (0001) basal texture are distributed along the ED and TD. As seen in Fig. 7d, when the tensile strain is 5%, the texture intensity is basically distributed along the ND.

With the addition of La-rich MM, as shown in Fig. 7e, the distribution of the (0001) basal texture changes little and the intensity value decreases to 8.97. Generally, adding RE elements to Mg and Mg alloys, such as La, Ce and Y, can apparently weaken the basal texture [15]. As seen in Fig. 7f, g, with the compressive strain increase to 2% and 4%, the texture features do not change much. The texture intensity of 4%-compressed sample is lower than that of the 2%-compressed. The reasons can be summarized as follow: (1) after further compression deformation, the grains are broken into finer grains, which rotate during deformation and the texture is dispersed. Meanwhile, more dynamic recrystallized grains are formed during compression, which leads to the weakening of texture. (2) A small amount of twins appear in the 4% compression sample, which also weakens the texture [16]. It can be seen that compressive deformation has little effect on the texture components of the extruded AZ110MM alloy. However, under the same deformation, adding La-rich MM to AZ110 alloy has a significant effect on the distribution of (0001) basal texture.

3.4 Mechanical Properties

The tensile and compressive mechanical properties curves of AZ110 and AZ110MM alloys are shown in Fig. 8. The specific data of the ultimate strength (US), yield strength (YS) and elongation (EL) are presented in Table 2. Compared with AZ110 alloy, the ultimate tensile strength and yield strength of AZ110MM alloy are significantly improved after the addition of La-rich MM. The CYS/TYS ratio is used to judge the tension and compression yield symmetry. The closer the ratio of CYS/TYS is to 1, the better the yield symmetry is. The yield strengths of the AZ110 alloy are 193 MPa in tension and 147 MPa in compression, resulting in a low CYS/TYS ratio (approximately 0.76). In contrast, the tensile and compressive yield strengths of the AZ110MM alloy are 281 MPa and 251 MPa, respectively, resulting in a relatively high CYS/TYS ratio (approximately 1.10). Definitely, the yield asymmetry of the extruded AZ110 alloy in this work is dramatically reduced by the addition of La-rich MM. Table 3 shows the summaries of the tensile and compressive properties of different alloys under specific processing in other studies [17–23]. As shown in Table 3, the AZ110MM alloy in this work has much higher compressive yield strength and better yield symmetry than those contrast alloys. Therefore, this alloy can meet the strength requirements of some industrial products. Meanwhile, Good tension symmetry can reduce the anisotropy of the alloy and make it more adaptable to different deformation modes.

4 Discussion

4.1 The Microstructure Variation with La-rich MM ADDITION

4.1.1 Grain Size

As shown in Fig. 4a, g, for the extruded AZ110 alloy, the addition of La-rich MM results in grain refinement. The possible reasons are ascribed to the synergistic effect of the

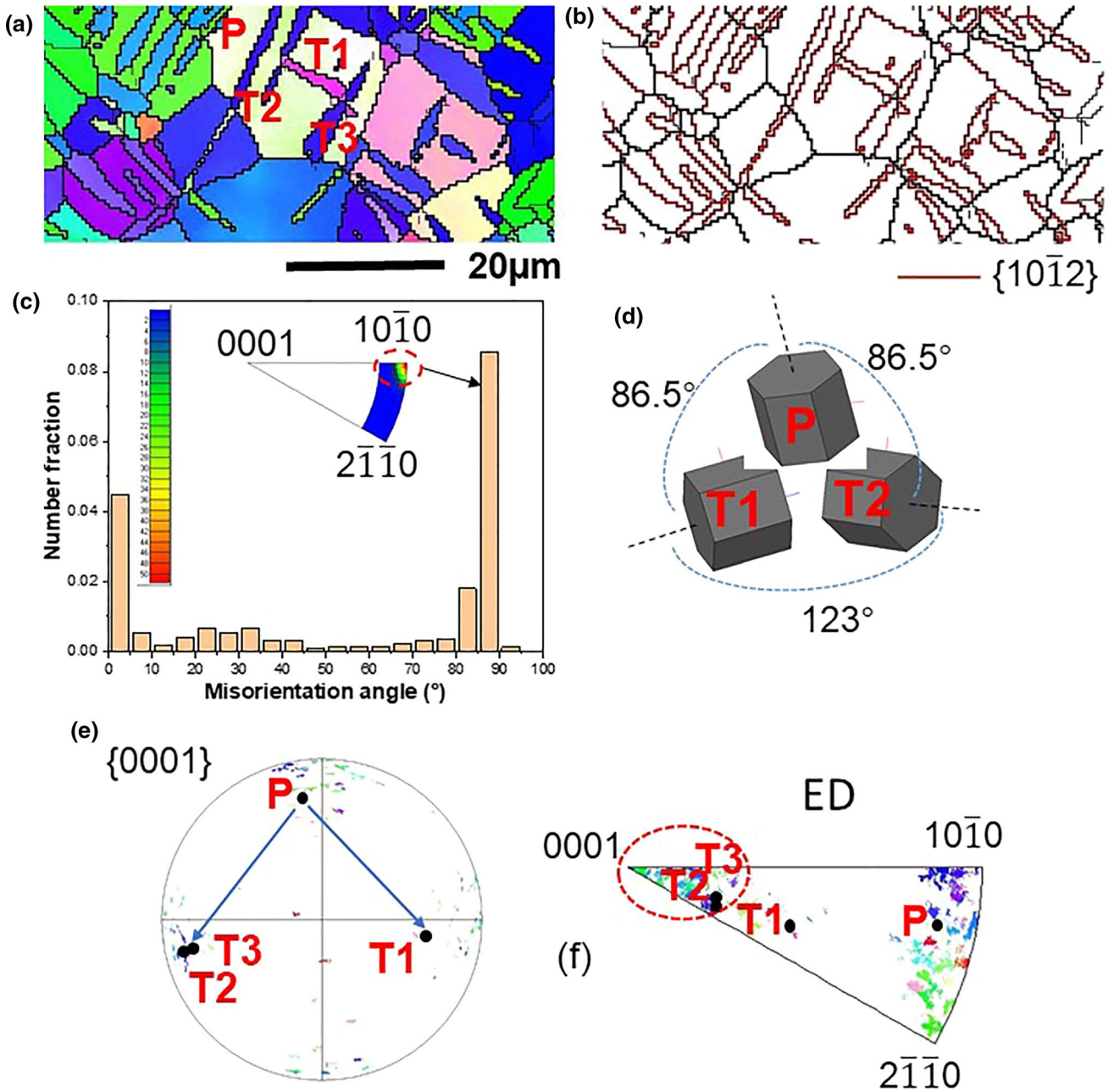

Fig. 6 EBSD results of the extruded AZ110 alloy under ~ 4% compressive deformation. **a** selected IPF map; **b** corresponding special boundary map; **c** misorientation angle distribution map; **d** the three-dimensional crystallographic relationship between {10$\bar{1}$2} extension twins and their parent grain. (T1, T2: {10$\bar{1}$2} extension twins; P: parent grain); **e** (0001) pole figure; **f** inverse pole figure;

following factors: (1) The Al-RE phases (Al_2(La, Ce) and Al_{11}(La, Ce)$_3$) precipitated in the Mg matrix could consume a certain amount of Al component, and the volume fraction of $Mg_{17}Al_{12}$ phase decreases. It is well known that $Mg_{17}Al_{12}$ phase can be softened when deformed above 573 K. While it is generally accepted that the Al-RE phases have the characteristics of thermal hardness and stability [24]. During extrusion, as shown in Fig. 9, dislocation accumulation frequently occurs in the vicinity of interfaces between Mg matrix and Al-RE phases. Those phases could increase more recrystallization nucleation cores and then the particle stimulated nucleation (PSN) phenomenon occurs to promote the refinement of recrystallized grain [25]. Zhang et al. [26] reported that with the addition of Ce/La elements, the original phases on the grain boundary are dispersed in the Mg matrix and the RE phases are fractured into fine particles which can hinder the grain growth during the recrystallization. On the other hand, Bu et al. [11] reported that the $Mg_{17}Al_{12}$ phase

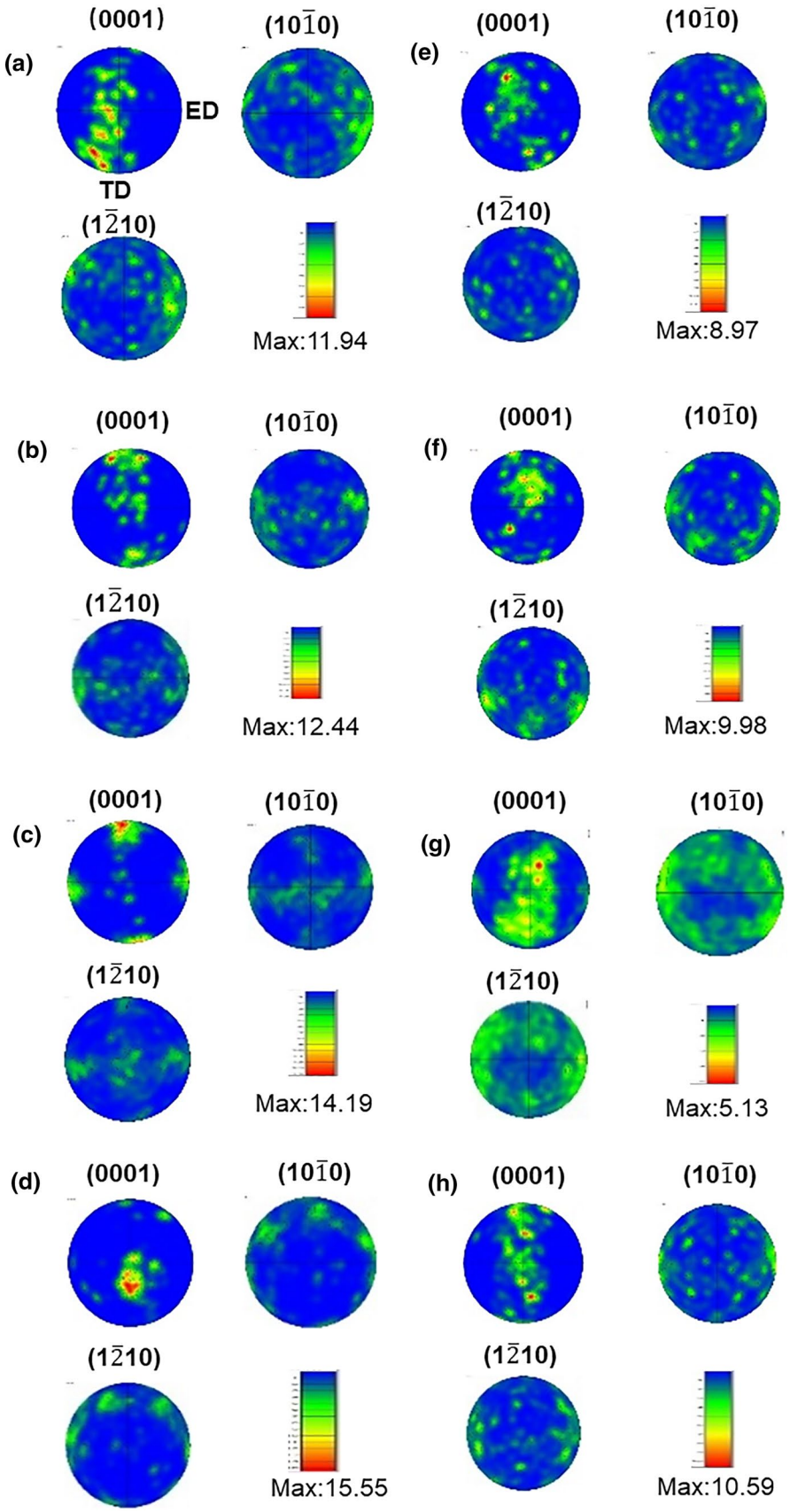

Fig. 7 Pole figures of the extruded AZ110 and AZ110MM alloys. AZ110 alloy: **a** initial extruded state; **b** 2% compressive strain; **c** 4% compressive strain; **d** 5% tensile strain; AZ110MM alloy: **e** initial extruded state; **f** 2% compressive strain; **g** 4% compressive strain; **h** 5% tensile strain

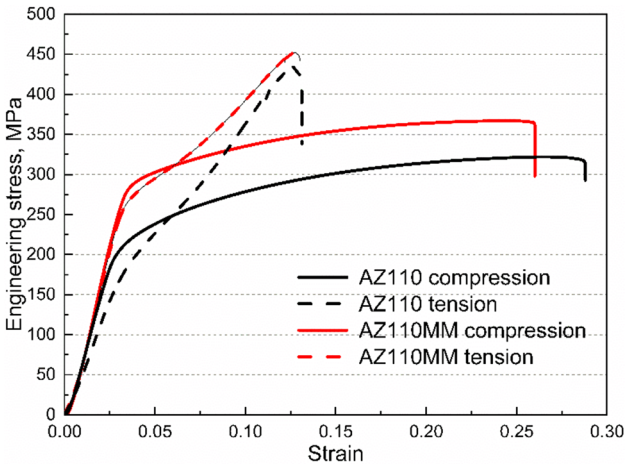

Fig. 8 Tensile and compressive mechanical properties of the extruded AZ110 and AZ110MM alloys

Table 2 Tensile and compressive properties of the extruded AZ110 and AZ110MM alloys

	AZ110		AZ110MM	
	Tension	Compression	Tension	Compression
US/MPa	323	428	368	451
YS/MPa	193	147	281	254
EL (%)	18.1	10.6	18.7	7.7

precipitated on the DRXed (dynamic recrystallized) grain boundaries also play an important role in restricting the growth of DRXed grains. However, the small fine and broken Al-RE particles would further impede the growth of newborn grains. (2) Before extrusion, the $Mg_{17}Al_{12}$ phase would be completely dissolved in the Mg matrix during homogenizing treatment, while the Al-RE phases always exist in the matrix. Therefore, during extrusion, the grain refinement effect of the Al-RE phases is more obvious. (3) As shown in Fig. 9, the Al-RE phases precipitated at the grain boundary exert strong dragging force on the grain boundaries motion and fine particles pinning the grain boundaries prevent the formation of lattice curvature necessary for nucleation [27].

4.1.2 Analysis of Twinning-Suppressed Behavior During Compression

As shown in Figs. 4e, k and 6, amount of $\{10\bar{1}2\}$ extension twins nucleate in the AZ110 alloy at 4% compressive strain, while no twins are observed in the AZ110MM alloy. It can be inferred that the Al-RE phases in the AZ110MM alloy play a significant role in suppressing the $\{10\bar{1}2\}$ extension twinning. For almost Mg alloys, the activation of the slip system and twinning must satisfy the condition that the shear stress along the particular direction at the specific slip plane (or twinning plane) should be greater than the critical resolute shear stress (CRSS), which can be represented as $\sigma_0 = \tau_{CRSS}/m$, where σ_0 is the yield strength for different conditions with texture variation, τ_{CRSS} is the critical resolute shear stress (CRSS) and m is the average value of the SF (Schmid factor) for the polycrystal. Table 4 shows the SF value of basal slip and $\{10\bar{1}2\}$ twin in the ED–TD plane under different tensile and compressive deformations. It is noted that the SF value of basal slip in AZ110 alloy during compression is lower than that of twinning and the stress required for twining-activation is lower. Therefore, the dominant deformation mechanism of the AZ110 alloy is twinning during compression. While basal slip is the dominated deformation mechanism during compressive deformation of AZ110MM alloy.

The possible reasons for the twinning-suppressed behavior in AZ110MM alloy during compression can be attributed to the synergy of the following factors: (1) there is a

Table 3 Summaries of tensile and compressive properties of different alloys under specific processing

Matrix	Properties		CYS/TYS	Processing	References
	TYS/MPa	CYS/MPa			
AZ31	140	110	0.79	Rolling	[16]
ZEK100	200 ± 7	150 ± 6	0.75	Extrusion	[16]
ZEK100 + 0.4%Ca	171 ± 2	148 ± 1	0.86	Extrusion	[17]
AZ80	200	149	0.75	Extrusion	[19]
AZ80–3.96%Sn	232	202	0.87	Extrusion	[19]
ZM21	212	171	0.81	ECAP	[20]
AM30	125	140	1.12	ECAP	[21]
AZ61	207	120	0.58	Extrusion	[22]
TZ51	182	133	0.73	Extrusion	[23]
AZ110	193	147	0.76	Extrusion	This work
AZ110MM	254	281	1.10	Extrusion	This work

(TYS: tensile yield strength; CYS: compressive yield strength; CYS/TYS: the ratio of CYS/TYS)

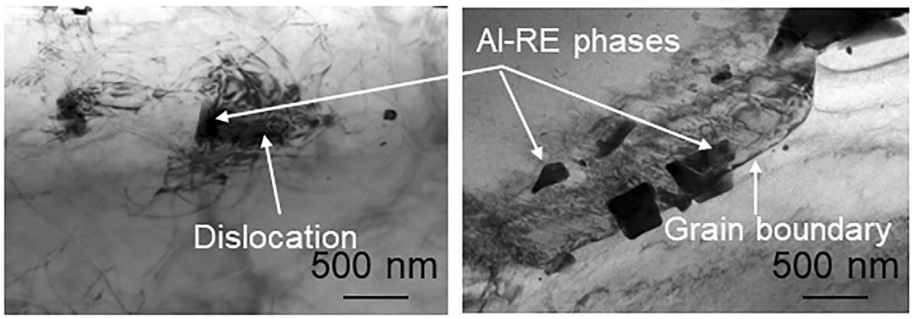

Fig. 9 Bright-field TEM micrographs of the extruded AZ110MM alloy

general agreement that smaller grain size inhibits twinning and grain size has a significant effect on the tendency of twinning since the energy required to form twin interfaces is particularly high in Mg alloys [17, 18]. The finer grains have a higher surface volume ratio, which increases the difficulty of twin nucleation and thus inhibits twins by limiting their size. As analyzed above, the AZ110MM alloy obtains fairly fine grains by adding La-rich MM. Meanwhile, finer grain size gives more uniform microstructure than the coarser grain sizes. The transition from finer grain size to coarse grain size corresponds to the slip-twinning transition. One possible reason for this is that the twinned lattice is more prone to flow localization than the un-twinned matrix. The wide variability of the grain sizes distribution which causes progressive twin nucleation [28, 29]. Therefore, grain refinement can be regarded as an important factor that affects the twinning nucleation. (2) The Al-RE phases could increase the value of τ_{CRSS} of the $\{10\bar{1}2\}$ extension twins, further hindering the twin formation in AZ110MM alloy. When the twins nucleate and approach the phases, there will be some back-stress resulted in the hard particles impeding the free shear of the moving twin ledge. This back stress must be conquered by adscititious stress. When the shear occurs at the interface between the matrix and the precipitates, the movement of atoms towards the precipitates must be regulated by basic slip [30, 31]. Therefore, the need for additional basal slip around the phases is likely to increase the stress required for twinning. Furthermore, with the La-rich MM addition, the basal texture of the extruded AZ110 alloy is weakened obviously. Seong-Gu Hong et al. [32] reported that the weakening basal texture could increase the difficulty of forming twins under lower compressive strain. As a result, the Al-RE phases in the AZ110MM alloy would modify potential twin nucleation sites and suppress the formation of twins.

4.2 Improved Tension–Compression Yield Asymmetry Achieved by La-rich MM Addition

The mechanical properties of the experimental alloys are shown in Fig. 8 and Table 3. It is revealed that the tension–compression yield asymmetry of the extruded AZ110 alloy is improved evidently by adding La-rich MM. Investigations of the microstructure of the AZ110 and AZ110MM alloys during tension and compression are instrumental in researching the details of the reduction in the tension–compression yield asymmetry [32, 33]. Generally speaking, the significant tension–compression yield asymmetry is originated from the deformation twinning polarity and the discrepancy of activated stress between deformation twinning and slip systems [34, 35].

Furthermore, grain size, texture and Al-RE phases have generally been regarded as the major factors associated with the yield asymmetry [29, 35]. The grain size dependence of extension twinning mode was found to be more pronounced than dislocation slip, and grain refinement could bring about more slip activity during compression, thus leading to the reduction of tension–compression yield asymmetry [36]. Therefore, the asymmetry of yield stress can be improved due to the grain refinement by adding La-rich MM to AZ110 alloy. Furthermore, texture could affect the tensile and compressive properties [37]. As shown in Table 4, when the compression deformation is 2%, the SF value of basal slip is lower than that of twin. In this case, it is difficult to activate basal slip. Meanwhile, this kind of orientation between grains and stress direction are not beneficial to the activation of pyramidal twinning either [38]. The intensive fiber texture with (0002) basal plane paralleling to the ED results in relatively high yield strength in tension along the ED of the AZ110 alloy. The compressive yield strength of the extruded AZ110 alloy is relatively low because its main deformation mechanism is twinning [38]. With the addition of La-rich MM, slip dominates the overall tension and compression deformation. The Al-RE phases restrain the exhibition of the $\{10\bar{1}2\}$ extension twins during compression, in which the CRSS for compression is larger than that of the RE-free sample. Because of this, the AZ110MM alloy maintains good consistency in the flow behavior at the elastic stage during tension and compression. Furthermore, the extruded Mg–Al–Zn systemic alloys with strong basal fiber texture show great yield asymmetry [39]. Extension twinning is easier to be activated than slip with strong basal texture during further twice deformation [39]. In terms of texture, the Al-RE

Table 4 Schmid factors of basal slip, $(10\bar{1}0)$ prismatic <a> slip in the ED–TD plane for AZ110 and AZ110MM alloys

	AZ110-tensile				AZ110MM-compression			
	As-extruded	Tens-5%	Comp-2%	Comp-4%	As-extruded	Tens-5%	Comp-2%	Comp-4%
m(bas)	0.26	0.18	0.21	0.18	0.28	0.20	0.24	0.34
m(twin)	0.30	0.34	0.34	0.28	0.15	0.13	0.18	0.20

phases can effectively reduce the yield asymmetry of the extruded AZ110 alloy. Additionally, as analyzed in the previous section, the Al-RE phases can suppress twinning-induced behavior. The RE phases distributed inside the grains can offer resistance to the propagation and growth of twins [40]. In this study, owning to grain refinement, texture modification and Al-RE phases, the tension–compression yield asymmetry of the extruded AZ110 alloy can be significantly improved by adding La-rich MM.

4.3 Strengthening Mechanism

In the present study, the AZ110MM alloy shows excellent strength properties due to the addition of La-rich MM. In order to quantify the effect of different strengthening mechanisms on the strength of the extruded AZ110MM alloy, the contribution values of these main strengthening mechanisms to the yield strength are calculated respectively. The strengthening mechanisms can be concluded as follows: (1) texture effect; (2) grain boundary strengthening; (3) solid solution strengthening; and (4) precipitation strengthening. It can be learned from the Hall–Petch relationship [41]: $\sigma_{0.2} = \sigma_0 + kd^{-1/2}$ ($\sigma_{0.2}$ is yield strength and σ_0 is the frictional stress for dislocation movement) that yield strength is directly related to grain size. Moreover, the results show that the texture also has a significant influence on the k value of the slip dominant deformation [38, 39]. The Schmid factors of the basal and prismatic slip of the two alloys were calculated and counted in detail. Figure 10 shows the quantitative analysis of <11–20> (0001) basal slip and <11–20> (10–10) prismatic slip of AZ110 and AZ110MM alloys. It can be seen that the Schmid factor of the prismatic slip is much larger than that of basal slip. However, the deformation mechanism of a small number of grains is still basal slip. We calculated the slip mode of each grain by calculating the Schmid factor of each grain <11–20> (0001) basal slip and <11–20> (10–10) prismatic slip. The percentage of texture strengthening by basal slip and prismatic slip of the two alloys was obtained. The value of Taylor factor was measured by EBSD software, which was suitable for overall deformation. Therefore, the formula for the effect of texture on yield stress is as follows [11]:

$$\Delta\sigma_t = (7.3\%M_{RE} - 15.7\%M_m)\tau^b_{CRSS} + (92.7\%M_{RE} - 84.3\%M_m)\tau^p_{CRSS} \quad (1)$$

where M is the Taylor factor for prismatic slip (M_m is for matrix alloy with a value of 2.23 and M_{RE} is for the AZ110MM alloy with a value of 2.63) and τ^b_{CRSS} and τ^p_{CRSS} are the critical resolute shear stress for the basal slip and prismatic slip of magnesium with value of 0.5 MPa and 39 MPa, respectively [42, 43]. Hence, the improved value for the texture effect is 21.6 MPa.

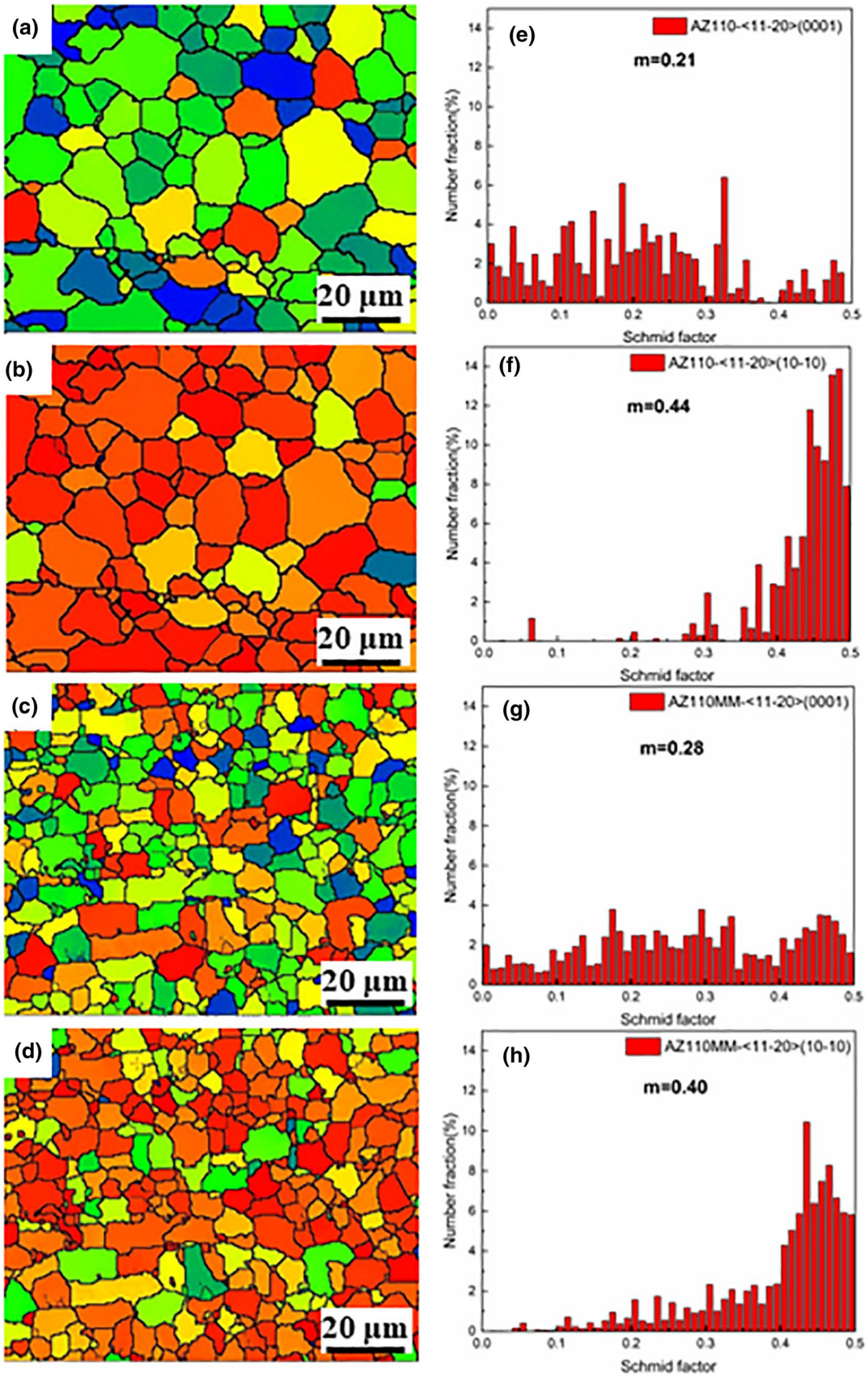
(a)
20 μm
(b)
20 μm
(c)
20 μm
(d)
20 μm
(e)
AZ110-<11-20>(0001)
m=0.21
Number fraction(%)
Schmid factor
(f)
AZ110-<11-20>(10-10)
m=0.44
Number fraction(%)
Schmid factor
(g)
AZ110MM-<11-20>(0001)
m=0.28
Number fraction(%)
Schmid factor
(h)
AZ110MM-<11-20>(10-10)
m=0.40
Number fraction(%)
Schmid factor

◂**Fig. 10** Quantitative analysis of <11–20> (0001) basal slip and <11–20> (10–10) prismatic slip of AZ110 and AZ110MM alloys. **a**, **e** AZ110—<11–20> (0001); **b**, **f** AZ110—<11–20> (10–10); **c**, **g** AZ110MM—<11–20> (0001); **d**, **h** AZ110MM—<11–20> (10–10)

Then, the grain boundary strengthening is contributed to grain refinement, which can be calculated by the following Hall–Petch equation [36, 43]:

$$\Delta\sigma_{gs} = k(d_{RE}^{-1/2} - d_{m}^{-1/2}) \tag{2}$$

where $\Delta\sigma_{gs}$ is the increment of yield strength caused by grain boundary strengthening, d_m and d_{RE} are the average grain sizes of the AZ110 and AZ110MM alloys, respectively, and assume that k is a constant value for given materials with a value of 210 MPa/μm$^{-1/2}$ [44]. Hence, the improved value for the grain boundary strengthening is 42 MPa.

Based on the Orowan mechanism [45], the Al-RE phases play a major role in relation to Orowan reinforcement. The phases have a strong pinning effect on the crystal lattice, which is beneficial to improve the yield strength. The equation can be expressed as [45]:

$$\Delta\sigma_{Orowan} = \frac{0.13Gb}{d_p\left[\left(\frac{1}{2f_v}\right)^{1/3}\right]}\ln\frac{d_p}{r} \tag{3}$$

where $\Delta\sigma_{Orowan}$ is the increment of Orowan strengthening, G is the shear modulus of the matrix with a value of 17.3 GPa for Mg [45], d_p is the particle size, r is dislocation core radius, b is the Burgers vector of gliding dislocations a value of 0.3196 nm, and f_v is the volume fraction of the Al-RE phases. If assuming r_0 = b, the improved value for precipitation strengthening effect is 26 MPa.

Lastly, the contribution of the solid solution to yield strength can be expressed by [46]:

$$\Delta\sigma_{ss} = 3.1\varepsilon CG^{1/2}/700 \tag{4}$$

where $\Delta\sigma_{ss}$ is the increment of the solid solution strengthening, ε is the experimental constant [46], and C is the solid solubility of La and Ce elements in at%. However, it is worth noting that the solid solubility of La and Ce elements in the Mg matrix is defective at a certain temperature, and the calculated value of solid solubility can be ignored.

Therefore, the yield strengthening equation can be written as:

$$\Delta\sigma_{0.2} = \Delta\sigma_t + \Delta\sigma_{gs} + \Delta\sigma_{Orowan} \tag{5}$$

As mentioned above, the calculated $\Delta\sigma_t$, $\Delta\sigma_{gs}$ and $\Delta\sigma_{Orowan}$ values of the AZ110 alloy are 21.6 MPa, 42 MPa, and 26 MPa, respectively. Grain boundary strengthening is the main strengthening mechanism for the AZ110 alloy with the addition of La-rich MM. This provides a reference method for improving the yield strength of Mg-based alloys.

5 Conclusion

The microstructure and mechanical properties of the extruded AZ110 alloy with the addition of La-rich MM were examined. The Al-RE phases have a significant effect on the regulation of microstructure and mechanical properties of the extruded AZ110 alloy. The key findings and conclusions are as follows:

(1) The RE phases in both as-cast and as-extruded AZ110MM alloy mainly consist of Al_2(La, Ce) and Al_{11}(La, Ce)$_3$. The Al-RE phases with thermal hardness and stability can exert strong dragging force on the grain boundaries motion and impede the growth of newborn grains, resulting in significant microstructure refinement of the AZ110 alloy during extrusion.

(2) The Al-RE phases inhibit the twin nucleation and growth through grain refinement and texture weakening, so that the cold compression deformation mechanism of the extruded AZ110 alloy change from twinning to multiple slip. The Al-RE phases can improve the tension–compression yield asymmetry performance of the extruded AZ110 alloy via the combining effects of grain refinement, texture weakening and the transformation from twinning to multiple slip.

(3) The yield strength of the extruded AZ110 alloy is significantly improved from 193 to 281 MPa with the addition of La-rich MM. The enhancement is mainly attributed to the texture effect, grain boundary strengthening and precipitation strengthening.

Acknowledgements This research was financially supported by the National Key Research and Development Program of China (Grant No. 2016YFB0301104) and State Key Laboratory of Baiyunobo Rare Earth Resource Researched and Comprehensive Utilization (Grant No. 2019Z2058).

References

1. I. Khoubrou, B. Nami, S.M. Miresmaeili, Met. Mater. Int. **26**, 196 (2020)
2. Q.Y. Liao, Q. Lan, W.T. Jia, X.R. Chen, Q.C. Le, T. Wang, J. Mater. Eng. Perform. **28**, 1977 (2019)
3. M.G. Jiang, C. Xu, H. Yan, G.H. Fan, T. Nakata, C.S. Lao, R.S. Chen, S. Kamado, E.H. Han, B.H. Lu, Acta Mater. **157**, 53 (2018)
4. L.B. Tong, M.Y. Zheng, S.W. Xu, X.S. Hu, K. Wu, S. Kamado, G.J. Wang, X.Y. Lv, Mater. Sci. Eng. A **528**, 672 (2010)
5. Q.Y. Liao, Q.C. Le, X.R. Chen, X.Q. Li, Y.C. Jiang, L.F. Ma, W.X. Hu, J. Mater. Res. Technol. **9**, 6777 (2020)

6. S.H. Park, J.H. Lee, B.G. Moon, B.S. You, J. Alloy. Compd. **617**, 277 (2014)
7. J. Bohlen, M.R. Nürnberg, J.W. Senn, D. Letzig, S.R. Agnew, Acta Mater. **55**, 2101 (2007)
8. Q. Zhang, T.W. Fan, L. Fu, B.Y. Tang, L.M. Peng, W.J. Ding, Intermetallics **29**, 21 (2012)
9. W.Q. Zhang, W.L. Xiao, F. Wang, C.L. Ma, J. Alloy. Compd. **684**, 8 (2016)
10. Y.C. Xin, X.J. Zhou, Q. Liu, Mater. Sci. Eng. A **567**, 9 (2013)
11. F.Q. Bu, Q. Yang, K. Guan, X. Qiu, D.P. Zhang, W. Sun, T. Zheng, X.P. Cui, S.C. Sun, Z.M. Tang, X.J. Liu, J. Meng, J. Alloy. Compd. **688**, 1241 (2016)
12. B.A. Esgandari, H. Mehrjoo, B. Nami, S.M. Miresmaeili, Mater. Sci. Eng. A **528**, 5018 (2011)
13. B. Nami, S.G. Shabestari, H. Razavi, Sh. Mirdamadi, S.M. Miresmaeili, Mater. Sci. Eng. A **528**, 1261 (2011)
14. Q. Yang, T. Zheng, D.P. Zhang, X.J. Liu, J. Fan, X. Qiu, X.D. Niu, J. Meng, J. Alloy. Compd. **572**, 129 (2013)
15. D.L. Zhang, H.M. Wen, M.A. Kumar, F. Chen, L.M. Zhang, I.J. Beyerlein, J.M. Schoenung, S. Mahajan, E.J. Lavernia, Acta Mater. **120**, 75 (2016)
16. X.Q. Li, C.L. Cheng, Q.C. Le, B. Lei, P.P. Jin, P. Wang, L. Ren, H. Wang, X. Zhou, C.L. Hu, J. Mater. Sci. Technol. **52**, 152 (2020)
17. S. Kamrani, C. Fleck, Mater. Sci. Eng. A **618**, 238 (2014)
18. C.F. Guo, Y. Xiao, R.L. Xin, Met. Mater. Int. **26**, 1366 (2020)
19. S.L. Lee, J.S. Kim, S.J. Park, S.H. Park, J.H. Yoon, Mater. Design **110**, 510 (2016)
20. E. Mostaed, A. Fabrizi, D. Dellasega, F. Bonollo, M. Vedani, J. Alloy. Compd. **638**, 267 (2015)
21. R. Jahadi, M. Sedighi, H. Jahed, Mater. Sci. Eng. A **593**, 178 (2014)
22. S. Kleiner, P.J. Uggowitzer, Mater. Sci. Eng. A **379**, 258 (2004)
23. B. Kim, S.M. Baek, H.Y. Jeong, J.G. Lee, S.S. Park, J. Alloy. Compd. **660**, 304 (2016)
24. J. Zhang, X. Niu, X. Qiu, K. Liu, C. Nan, D. Tang, J. Meng, J. Alloy. Compd. **471**, 322 (2009)
25. E. Oñorbe, G. Garcés, P. Pérez, P. Adeva, J. Mater. Sci. **47**, 1085 (2012)
26. J.B. Zhanga, L.B. Tong, C. Xu, Z.H. Jiang, L.R. Cheng, S. Kamado, H.J. Zhang, Mater. Sci. Eng. A **708**, 11 (2017)
27. F.A. Mirza, D.L. Chen, D.J. Li, X.Q. Zeng, Mater. Design **46**, 411 (2013)
28. O. Muránsky, M.R. Barnett, D.G. Carr, S.C. Vogel, E.C. Oliver, Acta Mater. **58**, 1503 (2010)
29. M.R. Barnett, Z. Keshavarz, A.G. Beer, D. Atwell, Acta Mater. **52**, 5093 (2004)
30. N. Stanford, M.R. Barnett, Mater. Sci. Eng. A **516**, 226 (2009)
31. J. Go, J.U. Lee, B.G. Moon, Y.H. Yoon, S.H. Park, Met. Mater. Int. **26**, 1779 (2020)
32. S.G. Hong, S.H. Park, C.S. Lee, Acta Mater. **58**, 5873 (2010)
33. Q. Tang, X.P. Lin, S.S. Zhao, Y. Niu, H. Sun, Y. Dong, Met. Mater. Int. **26**, 444 (2020)
34. L.X. Zhang, W.Z. Chen, W.C. Zhang, W.K. Wang, E. Wang, J. Mater. Process. Tech. **237**, 65 (2016)
35. M.R. Barnett, Scripta Mater. **59**, 696 (2008)
36. E. Dogan, I. Karaman, G. Ayoub, G. Kridli, Mater. Sci. Eng. A **610**, 220 (2014)
37. H.X. Wang, L.X. Zhang, W.Z. Chen, D.Q. Fang, W.C. Zhang, G.R. Cui, Mater. Sci. Eng. A **736**, 239 (2018)
38. Y.N. Wang, J.C. Huang, Acta Mater. **55**, 897 (2007)
39. S.M. Yin, C.H. Wang, Y.D. Diao, S.D. Wu, S.X. Li, J. Mater. Sci. Technol. **27**, 29 (2011)
40. Y. Jiang, Y.A. Chen, J.J. Gao, Mater. Design **105**, 34 (2016)
41. W.S. Huang, J.H. Chen, H.G. Yan, W.J. Xia, B. Su, W.J. Zhu, Met. Mater. Int. **26**, 747 (2020)
42. S.R. Agnew, C.N. Tome, D.W. Brown, Scripta Mater. **48**, 1003 (2003)
43. J.Y. Wang, M.A. Jon, J. Llorca, Acta Mater. **188**, 215 (2020)
44. H.H. Yu, Y.C. Xin, M.Y. Wang, Q. Liu, J. Mater. Sci. Technol. **34**, 248 (2018)
45. Z. Zhang, D.L. Chen, Scripta Mater. **54**, 1321 (2006)
46. R.W. Hertzberg, F.E. Hauser, J. Eng. Mater. Technol. **99**, 96 (1977)